Geol. Mag. **145** (*6*), *2008, pp. 845–857. © 2008 Cambridge University Press*
doi:10.1017/S0016756808005025 *Printed in the United Kingdom*

Geochronology and geochemistry of the *c.* 80 Ma Rutog granitic pluton, northwestern Tibet: implications for the tectonic evolution of the Lhasa Terrane

TAI-PING ZHAO*†, MEI-FU ZHOU‡, JUN-HONG ZHAO‡, KAI-JUN ZHANG* & WEI CHEN*

*Guangzhou Institute of Geochemistry, Chinese Academy of Sciences, Guangzhou, P.R. China
‡Department of Earth Sciences, The University of Hong Kong, Hong Kong, P.R. China

(*Received* 28 May 2007; *accepted* 11 December 2007; First published online 11 June 2008)

Abstract – The Rutog granitic pluton lies in the Gangdese magmatic arc in the westernmost part of the Lhasa Terrane, NW Tibet, and has SHRIMP zircon U–Pb ages of *c.* 80 Ma. The pluton consists of granodiorite and monzogranite with SiO_2 ranging from 62 to 72 wt % and Al_2O_3 from 15 to 17 wt %. The rocks contain 2.33–4.93 wt % K_2O and 3.42–5.52 wt % Na_2O and have Na_2O/K_2O ratios of 0.74–2.00. Their chondrite-normalized rare earth element (REE) patterns are enriched in LREE ((La/Yb)n = 15 to 26) and do not show significant Eu anomalies (δEu = 0.68–1.15). On a primitive mantle-normalized trace element diagram, the rocks are rich in large ion lithophile elements (LILE) and poor in high field strength elements (HFSE), HREE and Y. Their Sr/Y ratios range from 15 to 78 with an average of 30. The rocks have constant initial $^{87}Sr/^{86}Sr$ ratios (0.7045 to 0.7049) and slightly positive $\varepsilon_{Nd}(t)$ values (+0.1 to +2.3), similar to I-type granites generated in an arc setting. The geochemistry of the Rutog pluton is best explained by partial melting of a thickened continental crust, triggered by underplating of basaltic magmas in a mantle wedge. The formation of the Rutog pluton suggests flat subduction of the Neo-Tethyan oceanic lithosphere from the south. Crustal thickening may have occurred in the Late Cretaceous prior to the India–Asia collision.

Keywords: Late Cretaceous, I-type granite, Rutog, Gangdese magmatic arc, Lhasa Terrane.

1. Introduction

Mesozoic and Cenozoic igneous rocks are widely distributed in the Lhasa Terrane, where they form the Gangdese magmatic arc (Coulon *et al.* 1986; TBGMR, 1993; Yin & Harrison, 2000; Kapp *et al.* 2005). The arc is generally divided into the northern, central and southern belts (Pan, Wang & Li, 2002; Pan *et al.* 2006; Lu, Zhang & Ren, 2004). The southern and central belts have traditionally been interpreted as the result of northward low-angle subduction of Neo-Tethyan oceanic lithosphere beneath the Lhasa Terrane (Coulon *et al.* 1986; Hodges, 2000; Yin & Harrison, 2000). In contrast, the northern belt has been considered to reflect subduction of Palaeo-Tethyan oceanic lithosphere, now represented by the Bangong–Nujiang ophiolites, emplaced during collision between the Qiangtang and Lhasa terranes (Pan, Wang & Li, 2002; Pan *et al.* 2006).

The Rutog pluton in the westernmost part of the Lhasa Terrane belongs to the northern belt of the Gangdese arc. Our new geochronological data reveal that the intrusion is a Late Mesozoic body. Thus, study of this body can provide important clues to the origin of the Mesozoic igneous rocks in the Gangdese arc and their role in the tectonic evolution of the Tibetan Plateau.

†Author for correspondence: tpzhao@gig.ac.cn

In this paper, we present new SHRIMP zircon dates, whole-rock major and trace element data and Sr–Nd isotopic analyses for the Rutog pluton. This new dataset documents that the pluton was formed by partial melting of thickened continental crust. The melting was probably triggered by underplated basaltic magmas produced during northward subduction of Neo-Tethyan oceanic lithosphere.

2. Geological background

Tibet is an amalgamation of terranes accreted to the southern margin of Eurasia during the Phanerozoic (Chang & Zheng, 1973; Allègre *et al.* 1984). From north to south, it comprises the Qilian, Kunlun–Qaidam, Songpan–Ganzi, Qiangtang and Lhasa terranes, which are separated from one another by major suture zones marked by ophiolitic fragments and mélanges (Yin & Harrison, 2000). The Lhasa Terrane is separated from the Qiangtang Terrane to the north by the Bangong–Nujiang suture zone and from the Indian subcontinent to the south by the Yarlung–Zangbo suture zone (Fig. 1).

The Bangong–Nujiang suture zone, which extends for more than 1200 km across central Tibet, is marked by ophiolitic fragments and thick sequences of Jurassic flysch, mélange and volcanic rocks (Yin & Harrison, 2000). The Jurassic ophiolitic fragments along this belt are unconformably overlain by upper Jurassic–upper

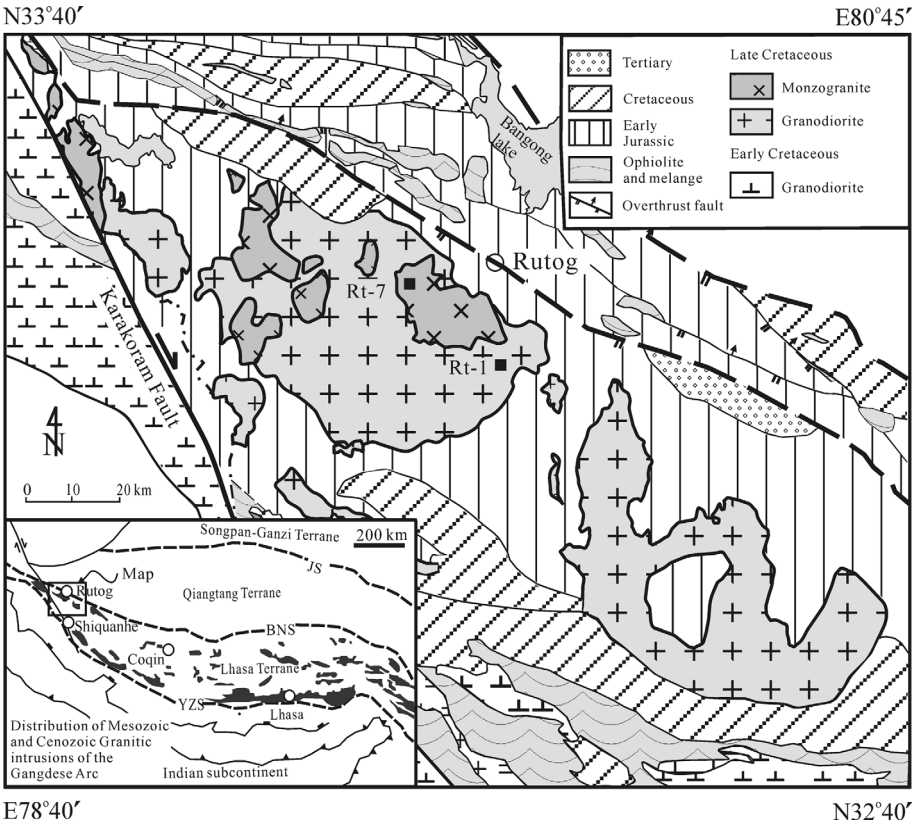

Figure 1. Simplified geological map of the Shiquanhe region, NW Tibet, showing the tectonic framework of the Tibetan Plateau (inset map) and the location of the Rutog pluton. JS – Jinshajiang suture; BNS – Bangong–Nujiang suture; YZS – Indus–Yarlung–Zangbo suture.

Cretaceous strata and were emplaced probably at *c.* 170 Ma (Zhou *et al.* 1997; Yin & Harrison, 2000). This ophiolitic belt is up to 100 km wide, probably reflecting the presence of intra-oceanic arc terranes (Pearce & Mei, 1988; Matte *et al.* 1996).

The Yarlung–Zangbo suture zone contains several well-preserved fragments of Neo-Tethyan oceanic lithosphere that were emplaced in the Cretaceous (Allègre *et al.* 1984; Aitchison *et al.* 2000). Final continent–continent collision, leading to the present configuration, probably occurred in Eocene times (Molnar & Tapponnier, 1975).

The Lhasa Terrane, 100 to 300 km wide, consists of a gneissic basement overlain by Palaeozoic to Cenozoic strata. Palaeozoic strata are represented by a sequence of Ordovician to Permian shallow marine sedimentary rocks (Yin & Harrison, 2000). Lower Cretaceous sedimentary rocks are locally overlain by early Tertiary volcanic sequences of the Linzizong Formation (Allègre *et al.* 1984; Murphy *et al.* 1997).

The Linzizong Formation, together with Cretaceous–Early Tertiary granitic batholiths, comprise the Gangdese arc in the Lhasa Terrane (Allègre *et al.* 1984; Coulon *et al.* 1986; Kapp *et al.* 2005). The volcanic rocks consist chiefly of calc-alkaline andesites and andesitic pyroclastic rocks, similar to those of the Andean continental-margin arc (Coulon *et al.* 1986; Mo *et al.* 2003).

Granitoids are widespread in the Shiquanhe area in the western part of the Lhasa Terrane (Fig. 1) and consist mainly of diorite and granodiorite. A muscovite-bearing granitic pluton intrudes Permian strata east of Shiquanhe. Synkinematic muscovite from a south-directed shear zone yielded a K–Ar age of 83 ± 4 Ma, which is believed to date reactivation of the suture zone near Bangong Lake (Ratschbacher *et al.* 1994). Ophiolitic mélange in Rutog has been thrust southward over lower Tertiary red beds, suggesting local shortening during the India–Asia collision (TBGMR, 1993).

3. Petrography of the Rutog pluton

The Rutog pluton is about 25–30 km wide and 190 km long, and crops out over an area of more than 3315 km^2 (TBGMR, 1993) (Fig. 1). It intrudes Lower–Middle Jurassic and Lower Cretaceous strata, and the contact is marked locally by dark hornfels (TBGMR, 1993). The intrusion is compositionally zoned, with an early, marginal phase of granodiorite and a later phase of biotite monzogranite. Abundant dioritic xenoliths and small pegmatitic dykes occur throughout the intrusion.

The granodiorites are coarse-grained and porphyritic in the central part to fine-grained and aphyric along the margins. They are mainly composed of quartz ($\pm$ 20 modal%), plagioclase ($\pm$ 50 %), K-feldspar ($<$ 10 %) and biotite + hornblende ($\pm$ 15 %). The plagioclase has well-developed oscillatory zoning, and some quartz grains contain needles of rutile.

https://doi.org/10.1017/S0016756808005025 Published online by Cambridge University Press

Table 1. SHRIMP zircon U–Pb analytical data for rocks from the Rutog pluton

Spot	$^{206}Pb_c$ %	U ppm	Th ppm	$^{232}Th/^{238}U$	$^{206}Pb^*$ ppm	$^{206}Pb/^{238}U$ age	$^{207}Pb/^{206}Pb$ age	$^{207}Pb^*/^{206}Pb^*$	±%	$^{207}Pb^*/^{235}U$	±%	$^{206}Pb^*/^{238}U$	±%
RT-1: granodiorite													
RT1.1	2.39	75.4	40.7	0.558	0.869	84.0 ± 2.2	−481 ± 590	0.0381	22	0.0690	22	0.0131	2.7
RT1.2	0.48	390	120	0.319	4.20	79.9 ± 1.7	−47 ± 91	0.0452	3.1	0.0777	4.3	0.0125	2.2
RT1.3	2.38	42.7	36.7	0.889	0.506	86.4 ± 2.4	−606 ± 450	0.0363	17	0.0680	17	0.0135	2.8
RT1.4	0.95	128	117	0.947	1.49	86.2 ± 2.0	−81 ± 210	0.0445	8.6	0.0827	9.0	0.0135	2.4
RT1.5	1.39	157	60.3	0.398	1.86	87.2 ± 2.0	−333 ± 240	0.0403	9.4	0.0756	9.7	0.0136	2.3
RT1.6	1.61	107	65.8	0.636	1.25	85.6 ± 2.1	−276 ± 310	0.0412	12	0.0759	13	0.0134	2.4
RT1.7	6.45	25.9	16.5	0.660	0.285	77.1 ± 2.9	−770 ± 1400	0.0340	50	0.0570	50	0.0120	3.8
RT1.8	1.09	57. 8	33.4	0.597	0.582	74.3 ± 1.9	82 ± 270	0.0477	11	0.0762	12	0.0116	2.6
RT1.9	3.17	22.7	15.2	0.691	0.255	80.9 ± 2.8	380 ± 690	0.0540	31	0.0940	31	0.0126	3.4
RT1.10	2.85	76.5	60.1	0.811	0.911	86.3 ± 2.3	−1108 ± 830	0.0305	27	0.0570	27	0.0135	2.6
RT1.11	4.10	28.2	18.9	0.695	0.324	82.3 ± 2.8	− 740± 1200	0.0350	42	0.0610	4.2	0.0128	3.4
RT1.12	2.79	54.8	45.2	0.851	0.601	79.5 ± 2.3	−609 ± 850	0.0360	31	0.0620	31	0.0124	2.9
RT1.13	2.75	50.1	29.1	0.601	0.533	77.4 ± 2.3	−696 ± 880	0.0350	32	0.0590	32	0.0121	2.9
RT1.14	1.45	83.2	50.5	0.627	0.922	81.5 ± 2.3	−190 ± 230	0.0426	9.2	0.0747	9.6	0.0127	2.8
RT1.15	3.22	46.1	27.3	0.611	0.511	80.0 ± 2.4	− 1080 ±1100	0.0310	36	0.0530	36	0.0125	3.0
RT1.16	3.35	52.9	31.8	0.620	0.560	76.4 ± 2.3	−940 ± 1000	0.0320	36	0.0530	36	0.0119	3.0
RT1.17	2.66	49.1	36.6	0.771	0.518	76.7 ± 2.4	−656 ± 580	0.0357	21	0.0590	21	.0.0120	3.1
RT1.18	0.229	88.9	81.2	0.945	1.03	86.2 ± 2.0	249 ± 120	0.0512	5.2	0.0950	5.7	0.0135	2.4
RT1.19	1.84	61.0	29.5	0.499	0.679	81.5 ± 2.1	−458 ± 460	0.0384	17	0.0670	18	0.0127	2.6
Rt-7: monzogranite													
RT7.1	0.298	138	115	0.859	1.37	73.9 ± 1.7	176 ± 95	0.0496	4.1	0.0788	4.7	0.0115	2.3
RT7.2	1.87	68.8	97.2	1.46	0.722	76.9 ± 2.3	117 ± 350	0.0484	15	0.0800	15	0.0120	2.9
RT7.3	0.781	121	85.7	0.730	1.30	79.2 ± 1.8	−187 ± 190	0.0427	7.7	0.0727	8.1	0.0124	2.3
RT7.4	0.587	177	125	0.726	1.78	74.6 ± 1.7	75 ± 110	0.0475	4.8	0.0762	5.3	0.0116	2.3
RT7.5	0.094	224	358	1.65	2.38	79.2 ± 1.8	155 ± 61	0.0491	2.6	0.0838	3.4	0.0124	2.2
RT7.6	0.337	253	351	1.44	2.70	79.4 ± 1.7	−37 ± 120	0.0453	5.0	0.0775	5.4	0.0124	2.2
RT7.7	1.51	51.0	39.0	0.790	0.546	78.7 ± 2.0	198 ± 280	0.0501	12	0.0850	12	0.0123	2.6
RT7.8	0.628	117	92.1	0.811	1.29	81.2 ± 1.9	−119 ± 24	0.0439	9.7	0.0767	10	0.0127	2.4
RT7.9	0.495	147	119	0.833	1.61	81.2 ± 1.8	−70 ± 140	0.0447	5.7	0.0782	6.1	0.0127	2.3
RT7.10	0.770	317	495	1.62	3.31	77.3 ± 1.7	61 ± 100	0.0472	4.3	0.0786	4.9	0.0121	2.2
RT7.11	0.694	184	195	1.10	1.98	80.1 ± 1.8	−130 ± 140	0.0436	5.7	0.0753	6.1	0.0125	2.3
RT7.12	1.14	96.7	80.7	0.862	1.11	84.5 ± 2.0	−144 ± 180	0.0434	7.2	0.0790	7.6	0.0132	2.4
RT7.13	0.425	102	91.2	0.923	1.15	83.6 ± 2.0	113 ± 190	0.0483	7.9	0.0868	8.2	0.0131	2.4
RT7.14	0.892	195	278	1.48	2.10	79.5 ± 1.8	−259 ± 170	0.0415	6.6	0.0710	7.0	0.0124	2.3
RT7.15	0.480	234	250	1.10	2.47	78.3 ± 1.7	−51 ± 72	0.0451	2.9	0.0760	3.7	0.0122	2.2
RT7.16	0.530	195	191	1.01	2.33	88.6 ± 2.0	30 ± 110	0.0466	4.7	0.0890	5.3	0.013	2.3
RT7.17	1.30	85.4	62.6	0.757	0.920	79.3 ± 1.9	25 ± 180	0.0465	7.4	0.0794	7.8	0.0124	2.4
RT7.18	0.583	102	70.5	0.715	1.10	79.9 ± 1.9	−34 ± 160	0.0454	6.5	0.0781	6.9	0.0125	2.4
RT7.1.1	0.355	355	724	2.11	3.25	68.1 ± 1.5	−68 ± 55	0.0448	2.2	0.0656	3.1	0.0106	2.2

Pb_C and Pb^* denote the common Pb and radiogenic Pb, respectively, while the common Pb was corrected using non-radiogenic ^{204}Pb.

The biotite monzogranite crops out mainly in the northern part of the intrusion (Fig. 1) and is hosted in the granodiorite. The monzogranite is coarse-grained and porphyritic, and consists of quartz (± 30 modal %), plagioclase (± 30 %), microcline perthite (± 25 %), biotite and hornblende (± 10 %). Accessory minerals include titanite, apatite, magnetite and zircon. The mineralogy suggests that these are I-type granites.

4. Analytical methods

4.a. SHRIMP zircon dating

Zircons were separated using magnetic and heavy liquid techniques, mounted in epoxy and ground to about half their thickness. Cathodoluminescence imaging was used to investigate the crystal zoning and to select analytical spots.

The zircon U–Pb dating was performed at the SHRIMP Ion Probe Centre, Chinese Academy of Geological Sciences, Beijing. The analytical procedures are described in Zhao *et al.* (2004). The standard zircon, Temora (417 Ma), was used to correct for elemental fractionation, and standard SL13 was used to monitor analytical precision. Common Pb was corrected using non-radiogenic ^{204}Pb. The programs SQUID 1.02 and ISOPLOT were used to reduce the data (Ludwig, 2001), and IUGS values (Steiger & Jäger, 1977) were used to calculate the ages. Uncertainties in Table 1 are reported at the 1σ level and the mean ages are reported at the 95 % confidence interval.

4.b. Major and trace element analyses

Samples from the Rutog pluton were analysed for major and trace elements at the Guangzhou Institute of Geochemistry, Chinese Academy of Sciences (Table 2). Samples were pulverized in a jaw crusher and then powdered in an agate mill to a grain size smaller than 160 mesh. Major oxides were determined using an X-ray fluorescence spectrometer (XRF) on glass discs, following the analytical procedures described by Goto & Tatsumi (1996). Analytical uncertainties for most major elements are estimated to be less than 1 %, based on repeated analyses of U.S.G.S. standards BHVO-2 (basalt), MRG-1 (basalt) and W-2 (diabase).

https://doi.org/10.1017/S0016756808005025 Published online by Cambridge University Press

Table 2. Major and trace element compositions for Rutog granites

Sample	RT-1	RT-2-1	RT-2-2	RT-3-1	RT-4-1	RT-4-2	RT-4-3	RT-5-1	RT-6-1	RT-7	RT-8	RT-9-1	RT-10-1	RT-10-2	RT-11
Major elements (wt%)															
SiO_2	65.66	67.84	68.39	69.46	69.56	70.06	71.31	70.61	68.5	67.93	72.13	69.52	68.04	61.71	63.36
TiO_2	0.75	0.47	0.51	0.44	0.23	0.45	0.37	0.48	0.51	0.51	0.39	0.50	0.56	0.88	0.91
Al_2O_3	16.26	16.09	15.65	15.81	16.82	14.86	14.52	14.61	14.91	16.28	14.67	15.03	15.37	17.04	15.37
Fe_2O_3	4.04	2.60	2.94	2.46	1.59	2.48	2.08	2.58	2.79	2.72	2.04	2.60	3.08	5.07	4.65
MnO	0.06	0.04	0.05	0.04	0.03	0.04	0.04	0.05	0.04	0.05	0.04	0.05	0.05	0.10	0.07
MgO	2.14	1.22	1.38	1.20	0.69	1.13	1.03	1.25	1.29	1.28	0.93	1.21	1.52	2.51	2.79
CaO	4.09	2.74	3.08	2.53	2.76	1.78	2.13	2.64	1.97	3.16	0.59	2.76	2.94	3.97	5.00
Na_2O	4.13	3.99	4.00	4.23	4.46	3.42	3.80	3.83	5.52	4.22	3.76	3.84	3.87	4.66	4.12
K_2O	2.44	4.17	3.41	3.64	3.83	4.63	4.12	3.58	2.97	3.60	4.93	3.66	4.01	2.33	3.51
P_2O_5	0.25	0.18	0.19	0.15	0.10	0.15	0.13	0.15	0.16	0.17	0.12	0.15	0.18	0.31	0.26
LOI	0.58	0.65	0.65	0.62	0.48	1.09	0.31	0.39	1.67	0.47	0.99	0.50	0.55	1.54	0.54
Total	100.40	99.99	100.24	100.57	100.54	100.09	99.86	100.17	100.33	100.38	100.59	99.81	100.17	100.09	100.59
ACNK	0.96	1.00	0.99	1.02	1.02	1.07	1.00	0.98	0.94	0.98	1.17	0.98	0.96	0.98	0.78
Trace elements (ppm)															
Sc	7.16	3.70	4.30	3.09	1.44	3.41	2.10	3.65	3.58	4.03	1.42	3.04	4.15	13. 5	7.46
V	76.9	41.6	43.1	40.0	24.7	39.2	37.0	41.6	56.7	42.6	34.4	43.1	55.7	73.5	81.0
Cr	18.3	9.4	8.8	9.1	5.8	9.1	14.1	12.1	11.7	nd	6.5	12.7	16.3	33.6	53.9
Ni	24.0	13.0	12.9	11.9	7.4	11.3	12.3	13.9	15.6	6.7	8.9	12.2	16.0	27.7	47.9
Co	9.8	5.8	6.2	5.2	3.4	6.2	4.7	6.1	6.1	5.9	3.8	6.0	7.1	12.7	13.4
Rb	72	154	134	136	153	138	163	137	112	157	202	164	151	137	149
Sr	463	332	305	287	408	299	249	283	289	355	185	308	313	355	441
Zr	96	141	151	113	97	134	116	132	130	138	110	129	155	295	189
Nb	11.9	12.2	12.4	12.1	6.7	12.5	10.5	14.6	11.9	13.4	15.2	15.3	15.8	26.1	20.8
Ba	407	474	254	253	472	401	270	231	292	327	298	427	429	177	417
Hf	2.63	3.77	4.15	3.12	2.85	3.84	3.10	3.58	3.39	3.62	3.03	3.79	4.18	7.37	4.97
Ta	0.89	1.10	1.07	1.16	0.63	1.18	0.84	1.28	0.98	1.35	1.32	1.53	1.41	2.48	1.65
Pb	12.1	20.2	16.9	16.5	22.2	19.8	18.4	14.5	9.9	22.1	64.3	20.4	20.2	13.2	12.1
Th	8.76	18.9	20.1	29.1	16.2	19.2	23.2	23.2	16.7	21.0	21.1	22.8	21.5	16.1	29.0
U	1.34	2.96	4.49	3.81	2.83	4.46	3.91	2.86	1.94	2.94	2.64	2.98	4.28	4.39	4.51
La	32.0	32.0	30.4	35.8	19.6	36.6	28.1	40.5	29.6	34.4	25.8	42.2	38.6	49.2	48.7
Ce	59.3	55.9	52.8	56.4	30.0	61.7	47.5	70.2	53.2	66.2	45.5	74.5	71.0	98.8	90.9
Pr	6.70	6.15	5.86	5.99	2.93	6.92	4.92	7.30	5.68	6.85	5.07	7.90	7.65	11.78	9.99
Nd	23.4	20.5	18.9	18.7	9.6	22.3	15.9	23.9	19.1	24.2	16.4	25.1	25.8	40.4	34.8
Sm	3.99	3.28	3.14	2.83	1.55	3.51	2.60	3.65	3.12	3.72	2.69	3.93	4.18	6.72	5.68
Eu	1.01	0.81	0.80	0.73	0.53	0.79	0.63	0.86	0.74	0.94	0.61	0.88	0.95	1.32	1.29
Gd	3.25	2.51	2.36	2.09	1.23	2.53	1.80	2.73	2.36	3.29	1.96	2.93	3.26	4.79	4.60
Tb	0.45	0.38	0.35	0.30	0.17	0.41	0.27	0.42	0.35	0.45	0.31	0.44	0.47	0.79	0.64
Dy	2.45	2.01	2.01	1.74	0.93	2.28	1.45	2.33	1.87	2.31	1.68	2.46	2.67	4.27	3.68
Ho	0.44	0.38	0.37	0.34	0.18	0.43	0.28	0.47	0.37	0.45	0.34	0.45	0.50	0.86	0.69
Er	1.21	1.04	1.03	0.95	0.52	1.19	0.77	1.29	1.04	1.23	0.93	1.30	1.37	2.26	1.89
Tm	0.17	0.16	0.16	0.15	0.08	0.18	0.12	0.20	0.15	0.19	0.14	0.20	0.21	0.36	0.26
Yb	1.12	1.09	1.07	0.98	0.60	1.24	0.80	1.28	0.99	1.27	1.01	1.31	1.40	2.34	1.73
Lu	0.17	0.18	0.18	0.16	0.10	0.19	0.13	0.21	0.16	0.21	0.16	0.20	0.21	0.37	0.25
Y	12.4	10.6	10.3	9.67	5.26	12.1	8.31	12.9	10.1	12.7	9.34	12.4	13.7	23.4	18.2

LOI – Loss On Ignition; ACNK – molecular ratio of $Al_2O_3/(CaO + Na_2O + K_2O)$.

The measured values of international standards are in satisfactory agreement with the recommended values.

Trace element data were obtained by Inductively Coupled Plasma-Mass Spectrometry (ICP-MS), following the analytical procedures described in Qi, Hu & Gregoire (2000). About 50 mg of rock powder were dissolved in distilled $HF–HNO_3$ in Savillex screw-top Teflon® beakers held at 150 °C for four days. Analytical precision for REE and HFSE is estimated to be 5 % from repeated analyses of U.S.G.S. standards, BHVO-1 and W-2.

4.c. Sr and Nd isotope analyses

For Sr–Nd isotopic analyses, sample powders (~ 100 mg) were dissolved overnight in distilled $HF–HNO_3$ using Savillex screw-top Teflon® beakers at 150 °C. Separation of Nd from the REE was carried out on HDEHP columns with a 0.18 N HCl elutant. The isotopic analyses were performed using a Micromass Isoprobe Multi-Collector ICP-MS, also at the Guangzhou Institute of Geochemistry.

Measured Sr and Nd isotopic ratios were normalized using a $^{86}Sr/^{88}Sr$ value of 0.1194 and a $^{146}Nd/^{144}Nd$ value of 0.7219. The Sr and Nd blanks were 0.5 and 0.3 ng, respectively. Analyses of standards gave the following results: NBS987 $^{87}Sr/^{86}Sr = 0.710243 \pm 14$ (2σ) and Shin Etou $^{143}Nd/^{144}Nd = 0.512124 \pm 11$ (2σ), equivalent to a value of 0.511860 for the La Jolla international standard (Tanaka *et al.* 2004).

5. Analytical results

5.a. SHRIMP zircon dating results

Zircons used for SHRIMP U–Pb dating were separated from a granodiorite (RT-1) and a monzogranite (RT-7). Zircons from the granodiorite (RT-1) are euhedral and prismatic with clear oscillatory zoning indicating

https://doi.org/10.1017/S0016756808005025 Published online by Cambridge University Press

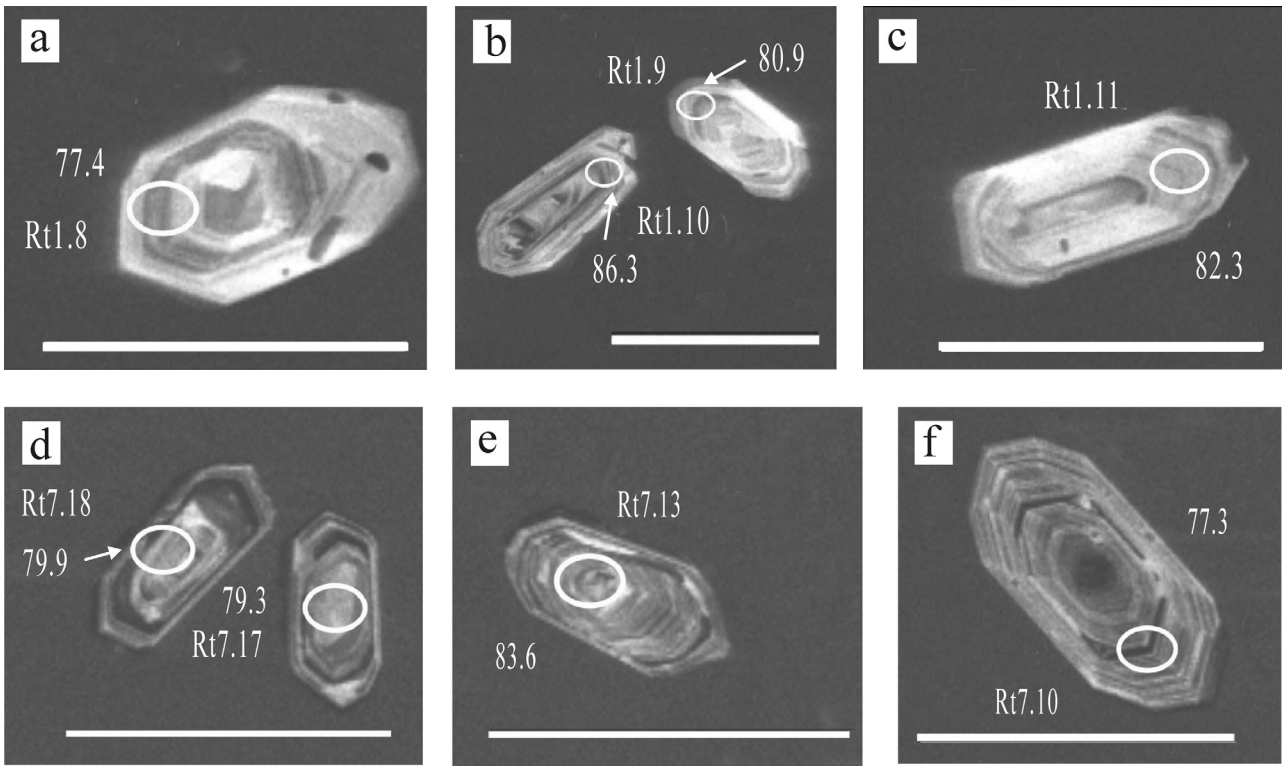

Figure 2. Cathodoluminescence images of zircons from the Rutog pluton. SHRIMP analysis points are white circles. The scale is 200 μm.

a magmatic origin (Fig. 2). These zircons have length to width ratios of 2:1 to 3:1.

Cathodoluminescence (CL) imaging reveals that there are some mineral inclusions (e.g. spots RT-1.5 and RT-1.6). A total of 20 analyses were obtained, with Th contents ranging from 15 to 120 ppm and U from 23 to 390 ppm, giving Th/U ratios of 0.32 to 0.95. The analytical results are listed in Table 1 and shown on concordia plots in Figure 3. Fourteen analyses from the inner and outer parts of different grains form a tight cluster with an average ^{206}Pb–^{238}U age of 80.0 ± 1.2 Ma. Six analyses yield slightly younger ^{206}Pb–^{238}U ages due to high U contents or loss of Pb.

Zircons from the monzogranite (RT-7) contain many inclusions and have well-defined magmatic zoning revealed by CL imaging (Fig. 2). Only those zircons without inclusions or inherited cores were selected for analysis. Nineteen analyses have Th contents ranging from 39 to 195 ppm and U contents from 51 to 317 ppm, yielding Th/U ratios of 0.71 to 1.61 (Table 1). Sixteen of the analyses plot near the concordia and yield ^{206}Pb–^{238}U ages ranging from 74.6 ± 1.7 Ma to 84.5 ± 0.2 Ma with a weighted average of 79.4 ± 0.9 Ma (Fig. 3). Two points have large errors in the ^{206}Pb–^{238}U ages, although they are still within the analytical uncertainties. One analysis (RT-7.1.1) has 355 ppm U, 724 ppm Th and 3.25 ppm Pb and yielded an age of 68.1 ± 1.5 Ma. The ratios of Pb/U and Pb/Th are 0.009 and 0.004, respectively, which are the lowest among all the zircons. This analysis is not included in the final calculation.

The granodiorite and monzogranite have identical ^{206}Pb–^{238}U ages of 80.0 ± 1.2 Ma and 79.4 ± 0.9 Ma, respectively, suggesting that the Rutog pluton formed in the late Cretaceous (*c.* 80 Ma).

5.b. Major and trace elements

Both the granodiorites and monzogranites have similar compositions, with SiO_2 ranging from 61.7 to 72.1 wt %, Al_2O_3 from 14.5 to 17.0 wt %, Fe_2O_3 from 1.59 to 5.07 wt % and MgO from 0.69 to 2.79 wt % (Table 2). Their K_2O ranges from 2.33 to 4.93 wt % and Na_2O from 3.42 to 5.52 wt %, yielding Na_2O/K_2O ratios of 0.7 to 2.0 (average of 1.2). They have Mg no. ranging from 12.0 to 15.9, with an average of 13.2. Most samples have A/CNK (molecular ratio of $Al_2O_3/(CaO + Na_2O + K_2O)$) values less than 1.1, indicating that they are Al-undersaturated. There are obvious negative correlations between SiO_2 and Fe_2O_3, TiO_2, MgO and CaO, and positive correlations between SiO_2 and K_2O (Fig. 4). These relationships suggest fractionation of ilmenite and plagioclase.

The rocks have high La (19.6 to 49.2 ppm) and low Yb (0.6 to 2.3 ppm), yielding high (La/Yb)n ratios of 15–26. They have LREE-enriched chondrite-normalized REE patterns with slightly negative Eu anomalies (δEu = 0.68–1.15) (Fig. 5). All samples are also enriched in LILE and depleted in HFSE, and display negative Nb–Ta and positive Zr–Hf anomalies in the primitive mantle-normalized trace element diagram (Fig. 6). They have relatively high Sr (163 to 185 ppm) and high Sr/Y ratios (15 to 78, average 30) (Table 2).

https://doi.org/10.1017/S0016756808005025 Published online by Cambridge University Press

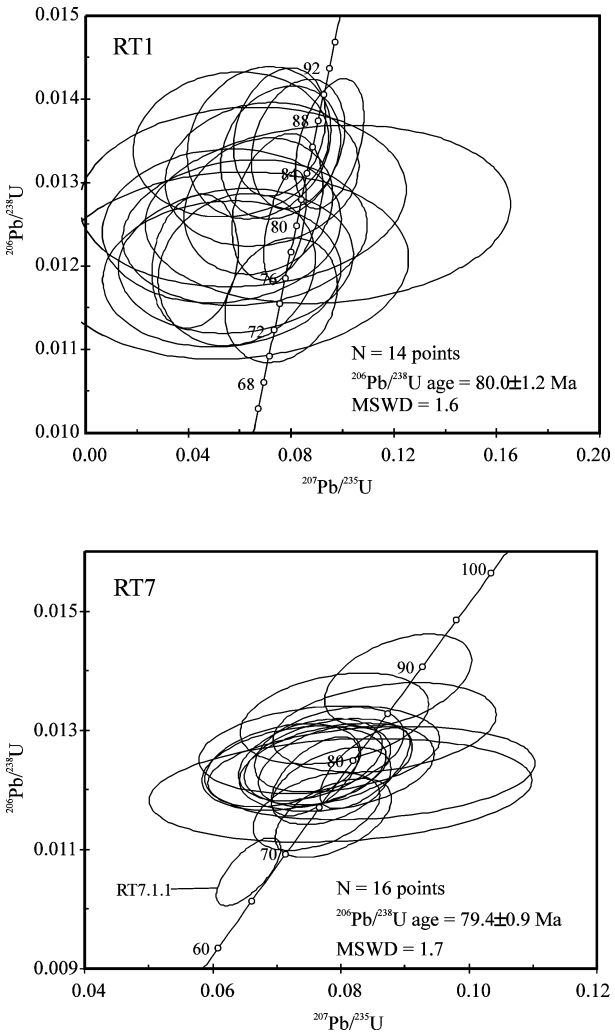

Figure 3. SHRIMP U–Pb concordia plots of zircons from the Rutog pluton.

5.c. Rb–Sr and Sm–Nd isotopes

Samples from the Rutog pluton have a wide range of $^{87}Rb/^{86}$ Sr ratios (0.45 to 3.15), but a narrow range of initial $^{87}Sr/^{86}Sr$ ratios (0.7045 to 0.7049) (Table 3). Their $f_{Sm/Nd}$ values range from −0.48 to −0.53, within the range of -0.4 ± 0.2 for corrected T_{DM} calculation (Wu *et al.* 2003*a*). Therefore, we use a single model age for the discussion. Their initial $^{143}Nd/^{144}Nd$ ratios range from 0.5125 to 0.5126 and ε_{Nd} (t = 80 Ma) values range from +0.1 to +2.3 with Nd model ages (T_{DM}) of 0.59–0.75 Ga. All samples have higher initial $^{87}Sr/^{86}Sr$ ratios than the mantle array in the plot of Sr versus Nd isotopes (Fig. 7).

6. Discussion

6.a. Classification of the Rutog granitic rocks

According to their protolith, granitic rocks are normally classified into I-, S-, M- and A-types (Chappell & White, 1974; Pitcher, 1982, 1993).

Chappell & White (1992, 2001) pointed out that I-type granites commonly display more regular linear variations in their chemical compositions than S-type granites, which generally display poor correlations between SiO_2 and P_2O_5 and between SiO_2 and Pb, different from I-type granitoids (Chappell & White, 1992). Well-defined linear trends in the Harker diagrams and a negative correlation between SiO_2 and P_2O_5 suggest that the Rutog rocks are unlikely to be S-type granitoids (Fig. 4).

I-type granitic rocks normally have high Na_2O, CaO and low Al_2O_3 and A/CNK values (molar $Al_2O_3/(CaO+Na_2O+K_2O) < 1.1$) compared to S-type granitoids, although there may be some overlap between them as observed in the Lachlan Fold Belt (Chappell & White, 2001). The relatively high Na_2O (3.42–5.52 wt %) and K_2O (2.33–4.93 wt %) and low Al_2O_3 (14.52 to 17.04 wt %) and aluminum saturation index A/CNK values (0.78 to 1.17) of the Rutog granitoids are consistent with an I-type classification. This classification is also supported by their low normative corundum (< 1.0 vol. %, except sample RT-8).

The Rutog granitoids do not contain mafic alkaline minerals such as arfvedsonite and riebeckite, and they have low concentrations of Na_2O+K_2O (6.57 to 8.69 wt %), low $(Na_2O+K_2O)/CaO$ (1.53–14.7), Fe_2O_3/MgO (1.67–2.30) and 1000 Ga/Al (1.82–2.39) ratios compared to A-type granitoids (Whalen, Currie & Chappell, 1987). They are also depleted in Nb, Zr, Ce and Y, again typical of I-type granitoids (Whalen, Currie & Chappell, 1987).

6.b. Magmatic differentiation

Fractional crystallization normally occurs during magma emplacement. The negative correlation between SiO_2 and MgO of the Rutog granitoids (Fig. 4) suggests accumulation/fractionation of mafic minerals

Table 3. Sr–Nd isotope compositions of rocks from the Rutog pluton

Sample	Rb ppm	Sr ppm	$^{87}Sr/^{86}Sr$	$^{87}Rb/^{86}Sr$	$(^{87}Sr/^{86}Sr)i$	Esr	Nd ppm	Sm ppm	$^{143}Nd/^{144}Nd$	$^{147}Sm/^{144}Nd$	$(^{143}Nd/^{144}Nd)i$	T_{DM}(Ga)	ε_{Nd}
RT-1	71.0	463	0.7055	0.4499	0.7049	7.7	23.4	3.99	0.512602	0.1029	0.512548	0.75	0.2
RT-2-1	154	332	0.7064	1.3436	0.7049	7.3	20.5	3.28	0.512593	0.0970	0.512542	0.73	0.1
RT-4-3	163	249	0.7070	1.8945	0.7048	5.7	15.9	2.60	0.512606	0.0990	0.512555	0.72	0.4
RT-5-1	137	283	0.7063	1.3971	0.7047	3.7	23.9	3.65	0.512600	0.0924	0.512551	0.69	0.3
RT-7	157	3559	0.7061	1.2833	0.7047	3.6	24.2	3.72	0.512650	0.0931	0.512601	0.63	1.3
RT-8	202	185	0.7085	3.1499	0.7049	6.7	16.4	2.69	0.512646	0.0991	0.512594	0.67	1.2
RT-10-1	151	313	0.7065	1.3991	0.7049	7.5	25.8	4.18	0.512627	0.0981	0.512576	0.69	0.8
RT-11	149	441	0.7057	0.9781	0.7046	2.5	34.8	5.68	0.512704	0.0988	0.512652	0.59	2.3

https://doi.org/10.1017/S0016756808005025 Published online by Cambridge University Press

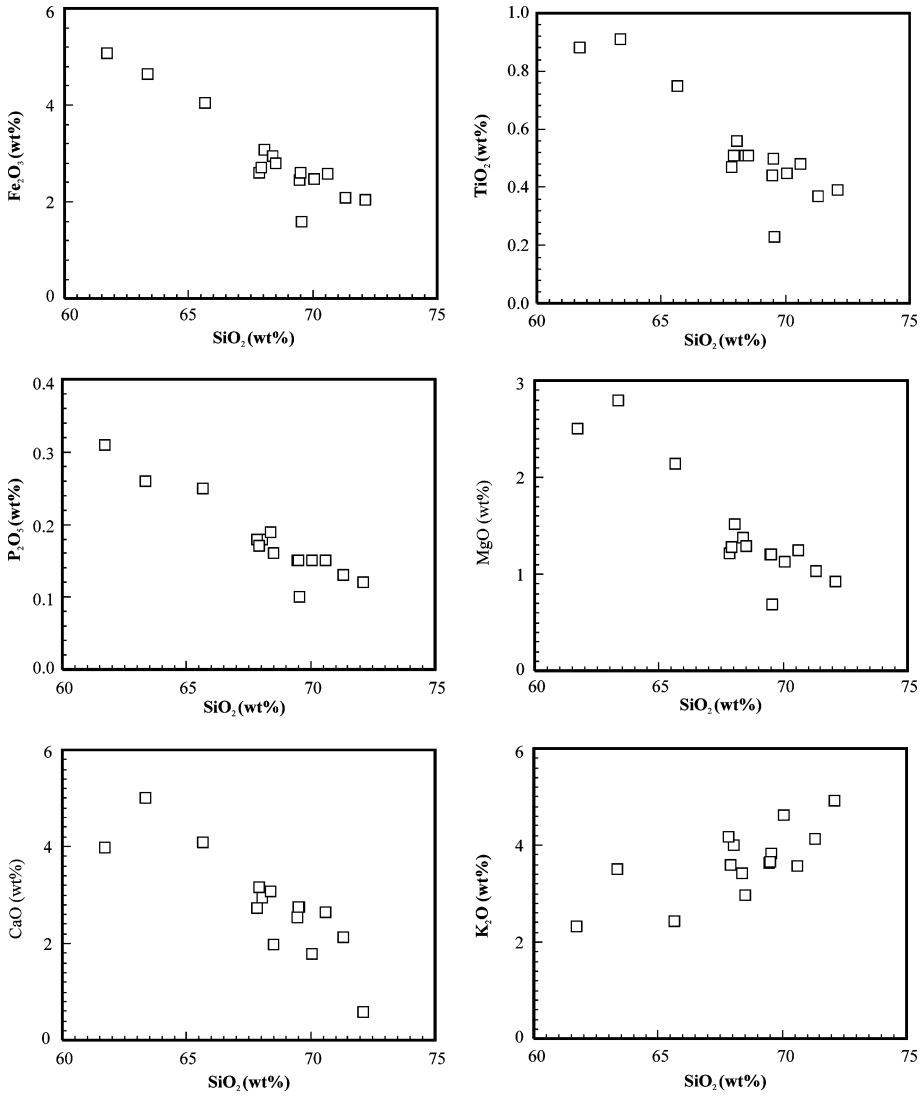

Figure 4. SiO_2 v. other major element oxides of rocks of the Rutog pluton.

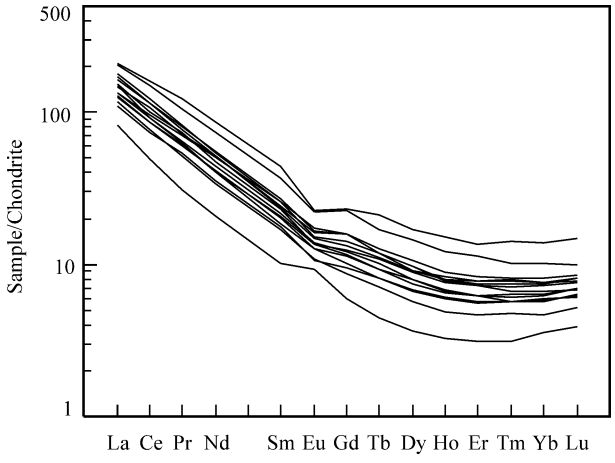

Figure 5. Chondrite-normalized REE patterns for rocks from the Rutog pluton. Normalization values are from Sun & McDonough (1989).

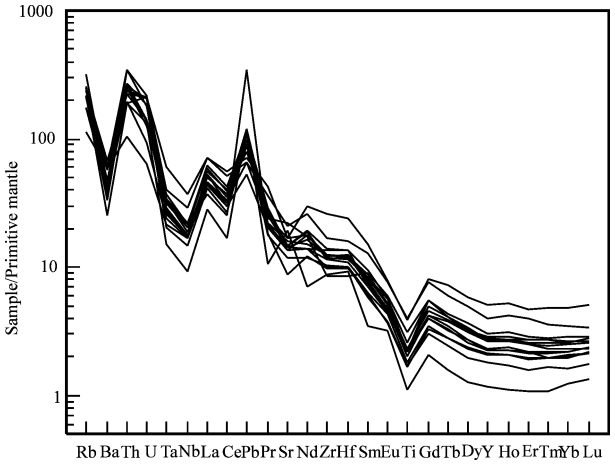

Figure 6. Primitive mantle-normalized trace-element diagram for rocks from the Rutog pluton. Normalization values are from Sun & McDonough (1989).

such as hornblende and biotite. Obvious Eu, Sr and Ba negative anomalies (Figs 5, 6) further demonstrate the fractionation of plagioclase (Wu *et al.* 2003*b*). A positive correlation between Sr and Ba (Fig. 8a) further indicates the fractionation of plagioclase (Li *et al.* 2007). There is only a weak correlation between Rb

https://doi.org/10.1017/S0016756808005025 Published online by Cambridge University Press

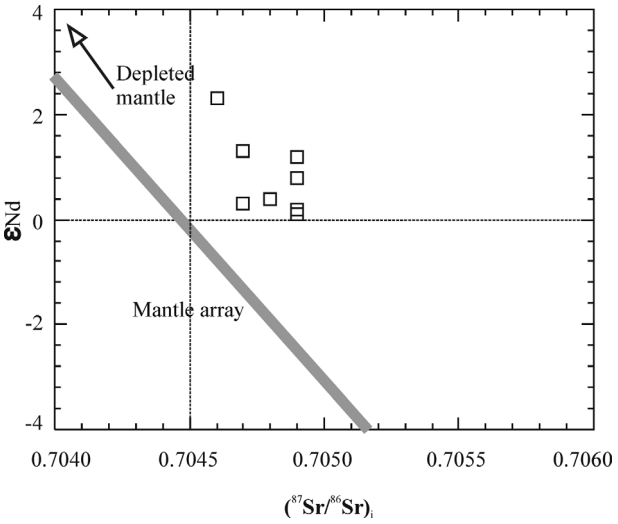

Figure 7. Plots of Sr–Nd isotopes for rocks from the Rutog pluton.

and Sr (Fig. 8b), suggesting that K-feldspar was not a fractionating mineral.

Separation of Ti-bearing minerals (such as ilmenite and titanite) and apatite lead to depletion of Nb–Ta–Ti

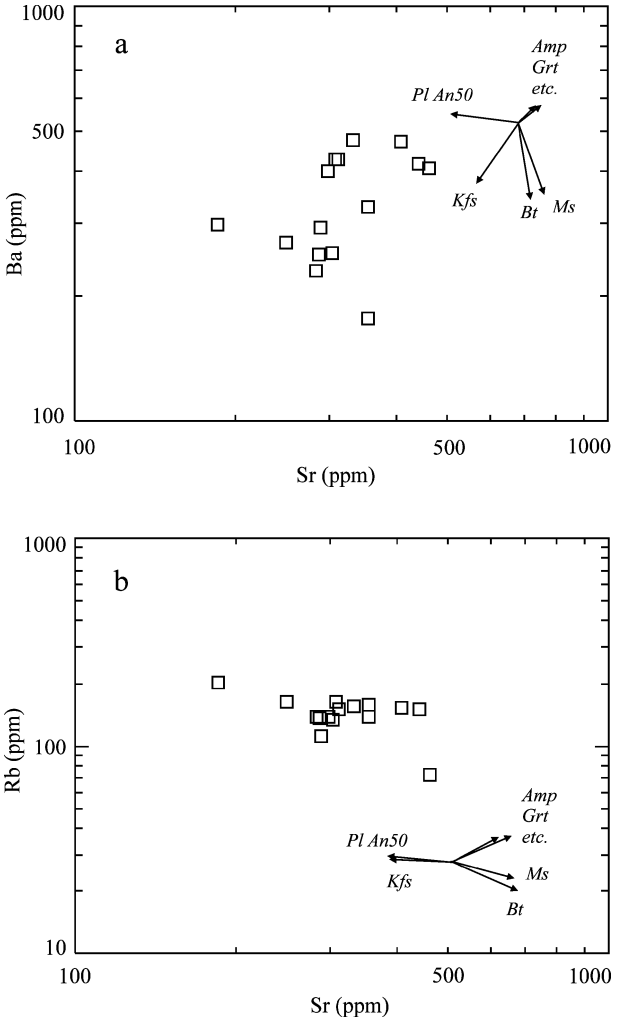

Figure 8. Fractional crystallization vector diagrams of Sr v. Ba (a) and Sr v. Rb (b) for the Rutog granites. The vectors are from Li *et al.* (2007).

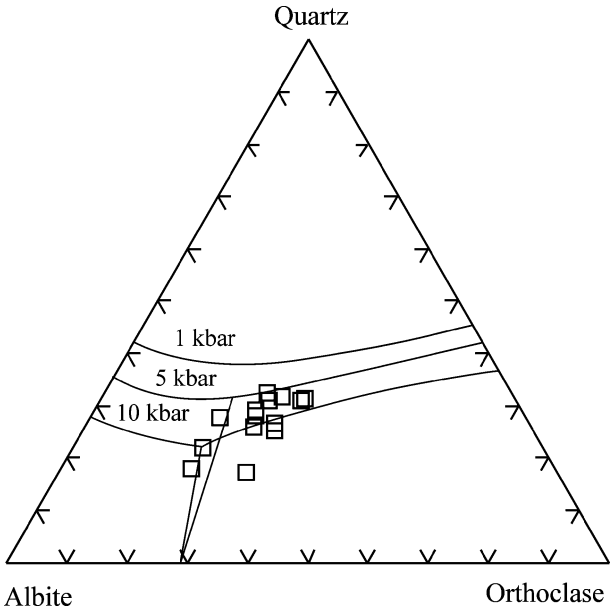

Figure 9. CIPW-normative Qz–Ab–Or diagram with low-temperature melt compositions at 1, 5 and 10 kbar (Johannes & Holtz, 1996).

and P, respectively (Wu *et al.* 2003*b*). The strong depletion of Nb–Ta–Ti of the Rutog rocks (Fig. 6) indicates fractionation of Ti-bearing phases, and the negative correlation of P_2O_5 with SiO_2 is consistent with fractionation of apatite.

In the CIPW-normative Qz–Ab–Or diagram (Fig. 9), most samples plot in the low-pressure field between 10 kbar and 5 kbar, and to the right of the cotectic/eutectic minima of the H_2O-saturated haplogranite system, typical of high-level emplacement of natural low-temperature granites (Johannes & Holtz, 1996), suggesting that the Rutog granodiorites were emplaced at pressures less than 1.2 GPa. This conclusion is also consistent with unidirectional growth of dendritic alkali feldspar (Shannon *et al.* 1982).

6.c. Petrogenesis of the Rutog pluton

It is well known that I-type granites can be produced by (1) mafic mineral fractionation at an early stage of mantle-derived magmas, (2) mixing between mantle and crustal melts and (3) partial melting of mafic crust.

Fractional crystallization during the early stages of mafic magma evolution may produce evolved felsic magmas (e.g. Litvinovsky *et al.* 2002). Although the Rutog granitoids experienced low-pressure fractional crystallization of amphibole and feldspars as discussed above, there is little evidence that the Rutog rocks were produced by differentiation of mantle-derived melts. Granitoids produced by differentiation of such melts should have model ages approximately similar to their emplacement age (e.g. Sun & Zhou, 2008). However, the Rutog granitoids have one-stage Sm–Nd modal ages (0.59–0.75 Ga) that are much older than their SHRIMP zircon U–Pb ages of *c.* 80 Ma. In

https://doi.org/10.1017/S0016756808005025 Published online by Cambridge University Press

addition, no mafic plutons have been identified in the region. Therefore, it is highly unlikely that the Rutog pluton was a product of differentiation from mafic magmas.

Mixing between mantle-derived mafic magma and crustal felsic melts can also produce I-type granites (Chappell, 1996; Yang *et al.* 2007). However, the Rutog granitoids have relatively homogeneous compositions, which are atypical of rocks formed by magma mixing. Rocks formed by magma mixing may have different types of zircon with distinct morphologies (Yang *et al.* 2007). Zircons from the Rutog pluton are all euhedral and prismatic with clear oscillatory zoning (Fig. 2), and two samples produce identical U–Pb ages (Fig. 3), suggesting that they were yielded from a homogeneous source region, rather than from mixing of mafic and felsic magmas. In addition, the Rutog rocks have relatively constant $^{87}Sr/^{86}Sr$ ratios (0.7045–0.7049), high $\varepsilon Nd(t)$ values (+0.1 to +2.3), and uniform REE and trace elemental patterns, all of which are inconsistent with a formation by magma mixing.

The Rutog rocks have T_{DM} ranging from 0.59 to 0.75 Ga, suggesting that they formed by melting of older crust. The relatively high $\varepsilon Nd(t)$ values and low $(^{87}Sr/^{86}Sr)_i$ ratios suggest that their protolith was derived from a depleted mantle source. The Gangdese granitoids and Linzizong volcanic rocks in the same region have similar $^{87}Sr/^{86}Sr$ ratios (0.704–0.705) and $\varepsilon Nd(t)$ values (+2 to +4) (Harris *et al.* 1988), indicating that they shared a common source region.

The Rutog rocks have Sr/Y ratios (15.2–78) and Y contents (8.31–23.4) transitional between normal arc and adakitic compositions (Fig. 10a). Three samples that have relatively high MgO and Y (Fig. 10b) and plot in the field of normal arc rocks can be explained by accumulation of amphibole, because amphiboles have relatively high Y contents (Castillo, Janney & Solidum, 1999). Partial melting of thickened, mafic continental crust (>40 km) under relatively high pressures normally produces adakites (Xu *et al.* 2002; Wang *et al.* 2005; Xiong, Adam & Green, 2005; Zhao & Zhou, 2008). Experiments have demonstrated that strongly fractionated adakite-like REE patterns, as well as low HREE contents, can only be generated from sources where garnet is stable under vapour-absent conditions at more than 1.2 Gpa (Rapp, Watson & Miller, 1991; Rapp & Watson, 1995; Sen & Dunn, 1994).

The temperatures of partial melting can be estimated by empirical equations for saturation temperatures of accessory mineral phases, such as monazite and zircon (Watson & Harrison, 1983; Rapp, Ryerson & Miller, 1987). Zr solubility is a function of the cation ratio ((Na +K+ 2Ca)/(Al∗Si)) and temperature in hydrous peraluminous or metaluminous melts (Fig. 11) (Watson & Harrison, 1983). Using this formula, we calculate that the Rutog granodiorites were produced at about 800 °C.

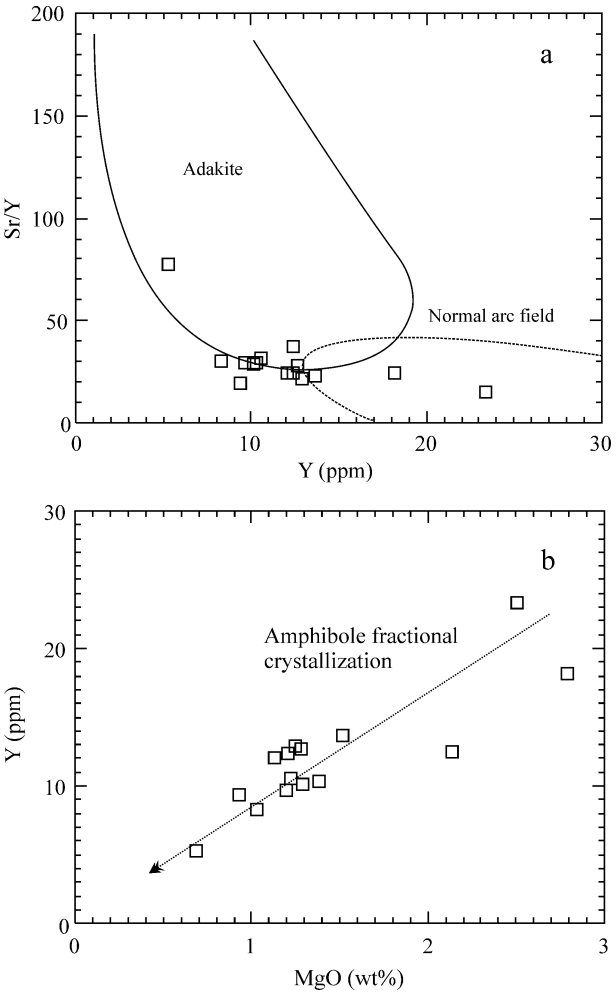

Figure 10. (a) Sr/Y v. Y for the rocks from the Rutog pluton. Fields for adakite or high-Al TTG and normal arc andesite and dacite are from Drummond & Defant (1990). (b) MgO v. Y for the rocks from the Rutog pluton showing the fractional crystallization of amphibole.

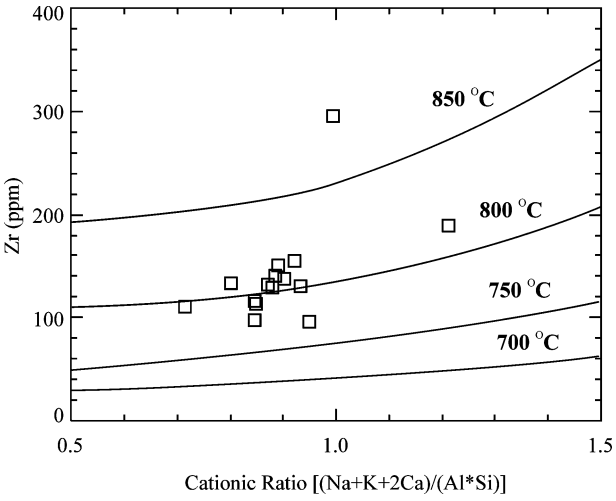

Figure 11. Plots of Zr concentration against the cation ratios of (Na+K+2Ca)/(Al∗Si) (Watson & Harrison, 1983).

Wu *et al.* (2003*a*,*b*) proposed a two-stage process to explain the highly fractionated I-type granites in NE China. We apply the same model to explain the petrogenesis of the Rutog pluton. In stage one, the

https://doi.org/10.1017/S0016756808005025 Published online by Cambridge University Press

parental magmas were generated by partial melting of the lower part of a thickened mafic crust and then underwent extensive differentiation at low pressures (5–10 kbar) and temperatures (800 °C) at a later stage.

6.d. Secular tectonic evolution of the Gangdese arc

6.d.1. Early Late Cretaceous crustal thickening in Tibet

Recognition of the *c.* 80 Ma Rutog I-type granitoids has significant implications for the tectonic evolution of the Gangdese arc and the Tibetan Plateau as a whole.

Accretionary orogeny in southern Tibet may have occurred in Late Cretaceous times. Significant upper crustal shortening of the Lhasa Terrane during the Cretaceous resulted in thickening of the continental crust. In the Coqin area, Murphy *et al.* (1997) documented >180 km of Cretaceous north–south shortening. The mid-Cretaceous Takena Formation near Lhasa experienced $\sim 40\,\%$ shortening prior to deposition of the overlying Linzizong volcanic rocks (Y. Pan, unpub. Ph.D. thesis, State Univ. New York, 1993). Large parts of the Lhasa Terrane experienced crustal shortening during Cenozoic times (Yin *et al.* 1994).

Cretaceous shortening and magmatism in central Tibet are attributed to northward underthrusting of the Lhasa Terrane beneath the Qiangtang Terrane along the Bangong–Nujiang suture zone during low-angle subduction of Neo-Tethyan oceanic lithosphere (Kapp *et al.* 2005). Thus, there might have been substantial crustal thickening in Tibet prior to the India–Asia collision, consistent with the occurrence of the Rutog pluton. Tertiary shortening in central Tibet may record continuous underthrusting of the Lhasa Terrane along the Bangong–Nujiang suture, which may have both accommodated, and been driven by, insertion of the Indian subcontinent into a previously thickened Tibetan crust (Kapp *et al.* 2003).

The Lower Cretaceous strata deposited in a flexural foreland basin are thought to have resulted from the Lhasa–Qiangtang collision (Yin *et al.* 1994). The occurrence of widely exposed Albian–Aptian shallow marine strata is taken as evidence that the Bangong–Nujiang suture zone was near sea level during mid-Cretaceous times (Kapp *et al.* 2003).

Thus, we infer that during the early Late Cretaceous, Tibet was situated in an accretionary convergent margin where orogenic processes involving arc magmatism, crustal thickening and rapid tectonic uplift may have been operating actively. This interpretation further suggests that accretionary orogeny took place in the Late Cretaceous and that a high mountain range in the northern part of the Lhasa Terrane in the Late Cretaceous already existed in Tibet prior to the India–Asia collision.

6.d.2. Post-orogenic origin and possible mechanism of melting

Crustal melting is dependent on the thickness and temperature of the crust. Granitic melts are generated

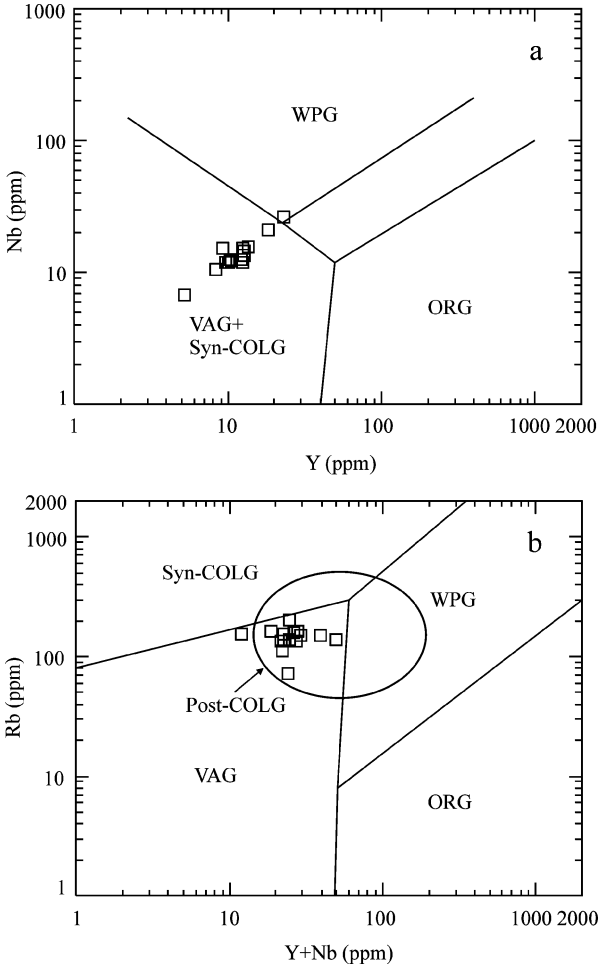

Figure 12. Plots of Y v. Nb (a) and Y+Nb v. Rb (b) for rocks from the Rutog pluton. Reference fields are from Pearce, Harris & Tindle (1984). Syn-COLG – Syn-collisional Granite; WPG – Within Plate Granite; ORG – Orogenic Granites; VAG – Volcanic Arc Granite.

where thickened crust is affected by (a) major crustal shears or thrusts (e.g., Barbarin, 1996), (b) *in situ* radiogenic heating from the over-thickened crust and (c) conductive heating from underplated magma in a post-collisional setting (e.g. Wang *et al.* 2007).

The negative Nb and Ti anomalies of the Rutog pluton are similar to those of syn-collisional granites in continental margins, indicating that the Rutog granitoids formed in a collisional environment (Pearce *et al.* 1984). On the Y v. Nb diagram, all of the Rutog samples plot in the field of volcanic arc granites (Fig. 12a), whereas on the Y+Nb v. Rb diagram they fall in the field of post-orogenic granitic rocks (Fig. 12b). In addition, all of the Rutog samples plot in the late orogenic field on the R_1–R_2 diagram (Fig. 13), suggesting that these rocks formed in a post-orogenic setting during early Cretaceous times.

We therefore propose that the Rutog pluton formed by crustal melting during continent–continent collision following closure of the Bangong–Nujiang Tethyan ocean. The emplacement of ophiolites along the Bangong–Nujiang suture zone may have occurred at 173 Ma (Zhou *et al.* 1997), and collision of the

https://doi.org/10.1017/S0016756808005025 Published online by Cambridge University Press

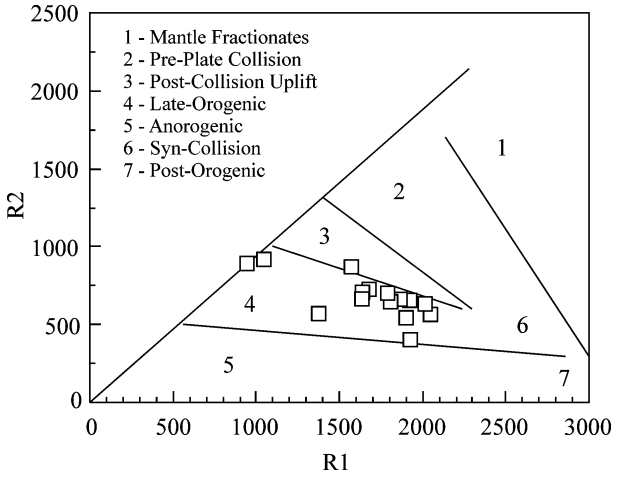

Figure 13. R_1–R_2 multi-cationic diagram of rocks from the Rutog pluton (after De la Roche *et al.* 1980). R_1 and R_2 are parameters calculated from chemical analyses, $R_1 = 4\text{Si} - 11(\text{Na}+\text{K}) - 2(\text{Fe}+\text{Ti})$ and $R_2 = 6\text{Ca} + 2\text{Mg} + \text{Al}$.

Qiangtang and Lhasa terranes occurred at least in the late early Cretaceous (about 100 Ma) (Pan, Wang & Li, 2002), 20 Ma earlier than the formation of the 80 Ma Rutog pluton.

Following closure of the ocean and crustal thickening, some areas of the orogen were invaded by mafic magmas, which promoted dehydration melting of the crustal rocks, generating large volumes of post-orogenic K-rich calc-alkaline granitic rocks including the Rutog pluton. The Sr–Nd isotopic compositions of these rocks indicate that the original magmas were mostly derived from juvenile Neoproterozoic arc material.

Partial melting of this crust was probably initiated by underplating of mafic magma above a flat subduction zone at *c.* 80 Ma. The wide distribution of Cretaceous arc magmatism in southern Tibet has led some workers to suggest that flat subduction occurred in the region before the India–Asia collision (e.g. Coulon *et al.* 1986).

7. Conclusions

The Rutog granitic pluton is a composite body with an age of 80 Ma. The Rutog rocks are geochemically I-type granitoids, and were formed by partial melting of a lower part of a thickened continental crust and emplaced at a shallow depth above a flat subduction zone from the south.

Acknowledgements. This work was supported by the CAS Hundred Talents Project (to ZKJ). The authors thank Ms Tao Hua for her assistance with the zircon SHRIMP U–Pb isotope analyses and Xu Yong-Hang for his help with the XRF and ICP-MS analyses. Zhang Yuxiu and Zhong Lifeng assisted with the field work. We thank Prof. Nick T. Arndt, Prof. Paul T. Robinson, and Dr Christina Y. Wang for their comments that helped to improve an early version of this paper. We also thank Dr Mark Allen and Mrs Jane Holland for their editorial work.

References

AITCHISON, J. C., BADENGZHU, D. A. M., LIU, J., LUO, H., MALPAS, J., MCDERMID, I., WU, H., ZIABREV, S. & ZHOU, M. F. 2000. Remnants of a Cretaceous intraoceanic subduction system within the Yarlung-Zangbo suture (southern Tibet). *Earth and Planetary Science Letters* **183**, 231–44.

ALLÈGRE, C. J. & 34 others. 1984. Structure and evolution of the Himalayan–Tibet orogenic belt. *Nature* **307**, 17–22.

BARBARIN, B. 1996. Genesis of the two main types of peraluminous granitoids. *Geology* **24**, 295–8.

CASTILLO, P. R., JANNEY, P. E. & SOLIDUM, R. U. 1999. Petrology and geochemistry of Camiguin Island, southern Philippines: insights to the source of adakites and other lavas in a complex arc setting. *Contributions to Mineralogy and Petrology* **134**, 33–51.

CHANG, C. F. & ZHENG, S. L. 1973. Tectonic features of the Mount Jolmo Lungma region in southern Tibet, China. *Scientia Geological Sinica* **1**, 11–2 (in Chinese with English abstract).

CHAPPELL, B. W. 1996. Magma mixing and the production of compositional variation within granite suites: evidence from the granites of Southeastern Australia. *Journal of Petrology* **37**, 449–70.

CHAPPELL, B. W. & WHITE, A. J. R. 1974. Two contrasting granite types. *Pacific Geology* **8**, 173–4.

CHAPPELL, B. W. & WHITE, A. J. R. 1992. I- and S-type granites in the Lachlan Fold Belt. *Transactions of the Royal Society of Edinburgh* **83**, 1–26.

CHAPPELL, B. W. & WHITE, A. J. R. 2001. Two contrasting granite types: 25 years later. *Australian Journal of Earth Sciences* **48**, 489–99.

COULON, C., MALUSKI, H., BOLLINGER, C. & WANG, S. 1986. Mesozoic and Cenozoic volcanic rocks from central and southern Tibet: $^{39}Ar/^{40}Ar$ dating, petrological characteristics and geodynamical significance. *Earth and Planetary Science Letters* **79**, 281–302.

DE LA ROCHE, H., LETERRIER, J., GRAND CLAUDE, P. & MARCHAL, M. 1980. A classification of volcanic and plutonic rocks using R1–R2 diagrams and major element analyses – its relationship with current nomenclature. *Chemical Geology* **29**, 183–210.

DRUMMOND, M. S. & DEFANT, M. J. 1990. A model for trondhjemite–tonalite–dacite genesis and crustal growth via slab melting: Archean to modern comparisons. *Journal of Geophysical Research* **95**, 21503–21.

GOTO, A. & TATSUMI, Y. 1996. Quantitative analyses of rock samples by X-ray fluorescence spectrometer (II). *Rigaku-Denki Journal* **13**, 20–39 (in Japanese).

HARRIS, N. B. W., XU, R. H., LEWIS, C. L., HAWKESWORTH, C. & ZHANG, Y. Q. 1988. Isotope geochemistry of the 1985 Tibet Geotraverse: Lhasa to Golmud. *Philosophical Transactions of the Royal Society, London* **A327**, 263–85.

HODGES, K. V. 2000. Tectonics of the Himalaya and southern Tibet from two perspectives. *GSA Bulletin* **112**, 324–50.

JOHANNES, W. & HOLTZ, F. 1996. *Petrogenesis and Experimental Petrology of Granitic Rocks.* Berlin: Springer, 335 pp.

KAPP, J. L. D., HARRISON, T. M., KAPP, P., GROVE, M., LOVERA, O. M. & DING, L. 2005. The Nyainqentanglha Shan: A window into the tectonic, thermal, and geochemical evolution of the Lhasa block, southern Tibet. *Journal of Geophysical Research* **110**, B08413.

KAPP, P., MURPHY, M. A., YIN, A., HARRISON, T. M., DING, L. & GUO, J. 2003. Mesozoic and Cenozoic

tectonic evolution of the Shiquanhe area of western Tibet. *Tectonics* **22**, 1029.

KAPP, P., YIN, A., HARRISON, T. M. & DING, L. 2005. Cretaceous–Tertiary shortening, basin development, and volcanism in central Tibet. *GSA Bulletin* **117**, 865–78.

LI, X. H., LI, Z. X., LI, W. X., LIU, Y., YUAN, C., WEI, G. J. & QI, C. S. 2007. U–Pb zircon, geochemical and Sr–Nd–Hf isotopic constraints on age and origin of Jurassic I- and A-type granites from central Guangdong, SE China: A major igneous event in response to foundering of a subducted flat-slab? *Lithos* **96**, 186–204.

LITVINOVSKY, B. A., JAHN, B. M., ZANVILEVICH, A. N. & SHADAEV, M. G. 2002. Crystal fractionation in the petrogenesis of an alkali monzodiorite–syenite series: the Oshurkovo plutonic sheeted complex, Transbaikalia, Russia. *Lithos* **64**, 97–130.

LU, S. W., ZHANG, L. & REN, J. D. 2004. Zonality of the Gangdese magmatic arc on the Qinghai–Tibet plateau and geological significance. *Geological Bulletin of China* **23**, 1023–32 (in Chinese with English abstract).

LUDWIG, K. R. 2001. *Squid 1.02: A user's manual.* Berkeley Geochronology Center, Special Publication no. 2, 19 pp.

MATTE, P., TAPPONNIER, P., ARNAUD, N., BOURJOT, L., AVOUAC, J. P., VIDAAL, P., LIU, Q., PAN, Y. & WANG, Y. 1996. Tectonics of western Tibet between the Tarim and Indus. *Earth and Planetary Science Letters* **142**, 311–30.

MO, X. X., ZHAO, Z. D., DENG, J. F., DONG, G. C., ZHOU, S., GUO, T. Y., ZHANG, S. Q. & WANG, L. L. 2003. Response of volcanism to the India–Asia collision. *Earth Science Frontiers* **10**, 135–48.

MOLNAR, P. & TAPPONNIER, P. 1975. Cenozoic tectonics of Asia; effects of a continental collision. *Science* **189**, 419–26.

MURPHY, M. A., YIN, A., HARRISON, T. M., DÜRR, S. B., CHEN, Z., RYERSON, F. J., KIDD, W. S. F., WANG, X. & ZHOU, X. 1997. Did the Indo-Asian collision alone create the Tibetan plateau? *Geology* **25**, 719–22.

PAN, G. T., MO, X. X., HOU, Z. Q., ZHU, D. C., WANG, L. Q., LI, G. M., ZHAO, Z. D., GENG, Q. R. & LIAO, Z. L. 2006. Spatial-temporal framework of the Gangdes Orogenic Belt and its evolution. *Acta Petrologica Sinica* **22**, 521–33.

PAN, G. T., WANG, L. Q. & LI, X. Z. 2002. The tectonic framework and spatial allocation of the archipelagic arc-basin systems on the Qinghai-Tibet Plateau. *Sedimentary Geology and Tethyan Geology* **21**, 1–26 (in Chinese with English abstract).

PEARCE, J. A., HARRIS, N. B. W. & TINDLE, A. G. 1984. Trace-element discrimination diagrams for the tectonic interpretation of granitic rocks. *Journal of Petrology* **25**, 956–83.

PIERCE, J. A. & MEI, H. 1988. Volcanic rocks of the 1985 Tibet Geotraverse Lhasa to Golmud. *Philosophical Transactions of the Royal Society, London* **A327**, 203–13.

PITCHER, W. S. 1982. Granite type and tectonic environment. In *Mountain Building Processes* (ed. K. J. Hsu), pp. 19–40. London: Academic Press.

PITCHER, W. S. 1993. *The Nature and Origin of Granite*. London: Blackie Academic and Professional, 321 pp.

QI, L., HU, J. & GREGOIRE, D. C. 2000. Determination of trace elements in granites by inductively coupled plasma-mass spectrometry. *Talanta* **51**, 507–13.

RAPP, R. P. & WATSON, E. B. 1995. Dehydration melting of metabasalt at 8–32 kbar: implications for continental growth and crust–mantle recycling. *Journal of Petrology* **36**, 891–931.

RAPP, R. P., RYERSON, F. J. & MILLER, C. F. 1987. Experimental evidence bearing on the stability of monazite during crustal anatexis. *Geophysical Research Letters* **14**, 307–10.

RAPP, R. P., WATSON, E. B. & MILLER, C. F. 1991. Partial melting of amphibolite/ecolgite and the origin of Archaean trondhjemites and tonalites. *Precambrian Presearch* **51**, 1–25.

RATSCHBACHER, L., FRISCH, W., LUI, G. & CHEN, C. 1994. Distributed deformation in southern and western Tibet during and after the India–Asia collision. *Journal of Geophysical Research (Part B)* **99**, 19817–945.

SEN, C. & DUNN, T. 1994. Experimental modal metasomatism of spinel lherzolite and the production of amphibole-bearing peridotite. *Contributions to Mineralogy and Petrology* **119**, 422–32.

SHANNON, J. R., WALKER, B. M., CARTEN, R. B. & GERAGHTY, E. P. 1982. Unidirectional solidification textures and their significance in determining relative ages of intrusions at the Henderson Mine, Colorado. *Geology* **10**, 293–7.

STEIGER, R. H. & JÄGER, E. 1977. Subcommission on geochronology: convention on the use of decay constants in geo- and cosmochronology. *Earth and Planetary Science Letters* **36**, 359–62.

SUN, S. S. & MCDONOUGH, W. F. 1989. Chemical and isotopic systematics of oceanic basalts: implications for mantle composition and processes. In *Magmatism in the ocean basins* (eds A. D. Saunders & M. J. Norry), pp. 313–45. Geological Society of London, Special Publication no. 42.

SUN, W.-H. & ZHOU, M.-F. 2008. The 860-Ma, Cordilleran-type Guandaoshan dioritic pluton in the Yangtze Block, SW China: implications for the origin of Neoproterozoic magmatism. *Journal of Geology* **116**, doi: 10.1086/587881, in press.

TANAKA, T. & 18 others. 2004. JNdi-1: a neodymium isotopic reference in consistency with La Jolla neodymium. *Chemical Geology* **168**, 279–81.

TBGMR (TIBETAN BUREAU OF GEOLOGY AND MINERAL RESOURCES,). 1993. Regional geology of Xizang (Tibet) Autonomous Region. Beijing: Geological Publishing House. *Geological Memoirs* 1(31), 699 pp. (in Chinese with English abstract).

WANG, Q., MCDERMOTT, F., XU, J. F., BELLON, H. & ZHU, Y. T. 2005. Cenozoic K-rich adakitic volcanic rocks in the Hohxil area, northern Tibet: lower-crustal melting in an intracontinental setting. *Geology* **33**, 465–8.

WANG, Y. J., FAN, W. M., SUN, M., LIANG, X. Q., ZHANG, Y. H. & PENG, T. P. 2007. Geochronological, geochemical and geothermal constraints on petrogenesis of the Indosinian peraluminous granites in the South China Block: A case study in the Hunan Province. *Lithos* **96**, 475–502.

WATSON, E. B. & HARRISON, T. M. 1983. Zircon saturation revisited: temperature and composition effects in a variety of crustal magma types. *Earth and Planetary Science Letters* **64**, 295–304.

WHALEN, J. B., CURRIE, K. L. & CHAPPELL, B. W. 1987. A-type granites: geochemical characteristics, discrimination and petrogenesis. *Contributions to Mineralogy and Petrology* **95**, 407–19.

WU, F. Y., JAHN, B. M., WILDE, S. A., LO, C. H., YUI, T. F., LIN, Q., GE, W. C. & SUN, D. Y. 2003*a*. Highly fractionated I-type granites in NE China (II): isotopic

geochemistry and implications for crustal growth in the Phanerozoic. *Lithos* **67**, 191–204.

WU, F. Y., JAHN, B. M., WILDE, S. A., LO, C. H., YUI, T. F., LIN, Q., GE, W. C., SUN, D. Y. 2003*b*. Highly fractionated I-type granites in NE China (I): geochronology and petrogenesis. *Lithos* **66**, 241–73.

XIONG, X. L., ADAM, J. & GREEN, T. H. 2005. Rutile stability and rutile/melt HFSE partitioning during partial melting of hydrous basalt: Implications for TTG genesis. *Chemical Geology* **218**, 339–59.

XU, J. F., SHINJIO, R., DEFANT, M. J., WANG, Q. & RAPP, R. P. 2002. Origin of Mesozoic adakitic intrusive rocks in the Ningzhen area of east China: partial melting of delaminated lower continental crust? *Geology* **32**, 1111–14.

YANG, J. H., WU, F. Y., WILDE, S. A., XIE, L. W., YANG, Y. H. & LIU, X.-M. 2007. Tracing magma mixing in granite genesis: in situ U–Pb dating and Hf-isotope analysis of zircons. *Contributions to Mineralogy and Petrology* **153**, 177–90.

YIN, A. & HARRISON, T. M. 2000. Geologic evolution of the Himalayan–Tibetan orogen. *Annual Review of Earth and Planetary Sciences* **28**, 211–80.

YIN, A., HARRISON, T. M., RYERSON, F. J., CHEN, W., KIDD, W. S. F. & COPELAND, P. 1994. Tertiary structural evolution of the Gangdese thrust system, southeastern Tibet. *Journal of Geophysical Research (Part B)* **99**, 18175–201.

ZHAO, T. P., ZHAI, M. G., XIA, B., LI, H. M., ZHANG, Y. X. & WAN, Y. S. 2004. Study on the zircon SHRIMP ages of the Xiong'er Group volcanic rocks: constraints on the starting time of covering strata in the North China Craton. *Chinese Science Bulletin* **9**, 2495–502.

ZHAO, J. H. & ZHOU, M. F. 2008. Neoproterozoic adakitic plutons in the northern margin of the Yangtze Block, China: Partial melting of a thickened lower crust and implications for secular crustal evolution. *Lithos* doi:10.1016/j.lithos.2007.12.009, in press.

ZHOU, M. F., MALPAS, J., ROBINSON, P. T. & REYNOLDS, P. H. 1997. The dynamothermal aureole of the Donqiao ophiolite (northern Tibet). *Canadian Journal of Earth Sciences* **34**, 59–65.